Single-cell differential detergent fractionation for detection of cytokeratin 8 proteoforms

Anna Fomitcheva Khartchenko[1], Trinh Lam[1], Amy E. Herr[1,2]*

1 University of California, Berkeley, USA

2 Chan Zuckerberg Biohub, USA

ABSTRACT: Simultaneous profiling of proteoforms and nucleic acids at the single-cell level, i.e., multi omics, directly links the central dogma. However, current single-cell approaches are limited in their ability to identify proteoforms while preserving the nucleus for further analysis. This limitation is especially pronounced in proteins where their proteoforms present diverse biological functions such as cytokeratin 8 (CK8), which, while commonly known for its structural role, is also involved in several diseases. Here, we present a single-cell western blot (scWB) integrated with differential detergent fractionation (DDF) to selectively solubilize and separate CK8 proteoforms while preserving nuclear integrity for subsequent nucleus-based assays. We report on assay development, including screening a panel of lysis buffers based on nonionic detergents and electrophoresis conditions to achieve a separation resolution between two proteoforms of up to 0.94 with an electric field of 30 V/cm, while preserving an intact nucleus. The cytoplasm-specific lysis approach (DDF buffer) demonstrated comparable solubilization efficiency to whole-cell solubilization (RIPA buffer), achieving proteoform solubilization in 14.3% and 10.3% of solubilized cells using DDF and RIPA buffers, respectively, while keeping the nucleus intact. To understand the broad applicability of the assay conditions, we scrutinized electrophoresis performance for resolving CK8 proteoforms across a panel of widely used breast cancer cell lines (MCF7, SKBR3, and MDA-MB-231), showing presence of proteoforms only in MCF7. Our approach allows for tailored solubilization, achieving reliable proteoform detection and nuclear retention across different cell types. Proteoform profiling at the single-cell level forms a basis for the exploration of the role of specific CK8 molecular forms in cellular processes.

Cytokeratin 8 (CK8) is an intermediate filament located in the cytoplasm and nucleus, that serves as a structural element and mediator of signal transduction. As a type II keratin it typically dimerizes with CK18[1], and is involved in various disease states. CK8 expression is modulated during viral infections, such as hepatitis C, influenza, and zika, with evidence suggesting a reorganization of the cytoskeleton to facilitate viral replication[2–4]. As product of *KRT8* gene mutations, CK8 may form amyloid-like aggregates linked to alcoholic liver disease[5]. Moreover, CK8 and its proteoforms have been implicated in cancer. Panels of cytokeratins have been used for the identification and diagnosis of certain cancer types such as bladder[6], lung[7], breast[8], and head and neck[9]. Notably, a CK8 proteoform in lung adenocarcinoma has been correlated with decreased survival[10]. In colorectal cancer, transcript-level CK8 revealed a clear differentiation of expression between tumor and normal tissue[11], highlighting the relevance of CK8 as a biomarker.

Currently, UniProt identifies two confirmed alternative-splicing derived isoforms of CK8 (#P05787), as well as six additional shorter forms, some of which are only computationally predicted[12]. At the transcript level, CK8 presents two isoforms. Recently, Li *et al* detected a new splicing variant, which corresponds to a predicted molecular mass of 46.2 kDa[11] (**Fig. 1A**), although its translation to protein remains uncertain, as no CK8 fragment with this molecular mass has been reported. The null observation suggests that this isoform is not translated into protein or that it is post-translationally cleaved into shorter forms. Previous studies provide evidence of CK8 cleaving events, yielding variable-length fragments of this protein[13]. The step between transcript to protein presents many intricacies, thus highlighting the need for new tools and strategies to analyze the presence of proteoforms as well as additional omic expressions.

To prepare a cell suspension for multiple analyses of targeted cellular compartments, compartment-specific assays have been appended to differential detergent fractionation (DDF) sample preparation approaches. DDF is a chemically targeted approach to selectively lyse cellular organelles, including the cytoplasm, nucleus, and various organelles. DDF mitigates non-specific background interference, commonly arising from cross-contamination between cellular compartments. Relevant for this study, DDF offers a cell compartment-specific fractionation of nuclear components for nucleic acid analysis versus cytoplasmic compartments for protein analyses. Bulk DDF methods use differential and density gradient centrifugation and magnetic beads to capture the organelles of interest[14,15]. These bulk approaches, however, mask single-cell heterogeneity. DDF has been adapted to single-cell compartment separations; for instance, single nuclei were maintained in microwells after selective lysis and electrophoresis of the cytoplasmic compartment[16–18]. Organelles can also be captured using antibodies against proteins common on the surface[19], or using centrifugal-based microfluidic devices that can separate cell debris from mitocondria[20,21]. The remaining intact nucleus or organelles are subsequently subjected to genomic analyses, chromatin studies, or nuclear protein assays.

Here, we sought to understand if we could develop a single-cell western blot optimized to resolve cytoplasmic CK8 proteoforms while keeping each cell's nucleus intact. Given our interest in breast cancer biology and the need to benchmark assay performance across model systems, we applied the CK8 isoform-optimized single-cell western blot (scWB) to a panel of breast cancer cell lines.

Experimental Section

SU-8 mold fabrication

Molds for soft lithography were fabricated as previously described[19]. A layer of SU-8 3050 was spun over a silicon wafer for 10 s at 500 rpm with an acceleration of 100 rpm, and then for 30 s at 4000 rpm with an acceleration of 300 rpm to achieve a layer thickness of 40 µm. The wafer was soft baked for 2 min at 65°C, 15 min at 95°C and then 3 min at 65°C. The wafer was exposed to a UV dose of 385 mJ/cm^2 and then baked post-exposure for 1 min 65°C, 5 min at 95°C and then 1 min at 65°C. The wafer was developed for 5 min on a shaker and then hard baked at 200°C for 20 min.

Single-cell western blot

The scWB was performed as previously reported[22]. Briefly, gels were fabricated mixing 7% acrylamide:bis-acrylamide (29:1, Sigma-Aldrich), 3 mM BPMA (BP-APMA, custom synthesis by Raybow Pharmaceutical), 0.08% ammonium persulfate (Sigma Aldrich), and 0.08% tetramethylethylenediamine (Sigma Aldrich). The solution was then incorporated between a wafer and a silanized glass slide[22] until the end of polymerization after 15 min, when the gel was detached from the wafer and deposited in PBS for 1h. The gel was then dried under a nitrogen stream, and 250 µL pf 1 million/mL of strained cells were deposited on the gel for cell settling. After 10 min, the excess cells were removed with PBS, and the gels were placed in the Milo system (Protein Simple, Bio-Techne) for electrophoresis. The lysis and electrophoresis times, and the electric field were adjusted on an experimental basis, with lysis 30 s and electrophoresis 30 s unless otherwise noted. The photoactivation time was set to 45 s. After the electrophoresis step, the gel was deposited in 1x Tris Buffered Saline + 0.1% Tween-20 (TBST) for 1h. The gel was then incubated with primary antibody for 1 h, washed in TBST for 45 min with one wash exchange after 20 min, and incubated with the secondary antibody for 1h. The sample was washed in TBST for 45 min with one wash exchange, and then rinsed in water to remove salts. The gel was dried under a nitrogen stream and imaged using Genepix Microarray Scanner (Genepix 4300A, Molecular Devices), with a resolution of 5 µm. The channel 535 used a laser power of 90% and a gain of 500, and channel 635 used a laser power of 70% and a gain of 700.

Primary antibodies were β-tubulin (100 µg/mL, ab6046 Abcam), CK8 (2.5 µg/mL, ab9023 Abcam), histone H3 (100 µg/mL, ab1791 Abcam) and secondary antibodies were anti-rabbit-633 (A21071 Thermo Fisher) and anti-mouse-532 (A11002 Thermo Fisher), all at 100 µg/mL. DNA was stained using SYBR gold at the suggested concentration (S11494 Thermo Fisher).

Data analysis was performed using a Python custom algorithm based on ref.[23], using numpy, pandas, tkinter, and pillow. Briefly, the images were cut into single bands, a thresholding function was used for segmentation of the band, and the intensity was extracted. Plotting was performed using Prism. Statistics were performed using the Kruskal-Wallis test for non-parametric datasets. The scWB micrographs presented here are inverted grayscale and contrast-adjusted for visualization.

Buffer composition

The RIPA buffer composition used was 1% w/v SDS, 0.5% w/v sodium deoxycholate, 0.1% v/v Triton-X100, and 0.5x of Tris Glycine. The cytoplasmic base buffer composition was 1% v/v Triton X-100, 0.125 mg/mL digitonin 99% pure, and 0.5x Tris Glycine. Buffers from **Fig. 2** were formulated by adding the described w/v (DDM, urea (both Sigma Aldrich)) or v/v (Brij-35 (Thermo Fisher), IGEPAL (Abcam)) of the detergent in the cytoplasmic base buffer (**SI Table 1**).

Top-down mass spectrometry

The fractions of proteins were obtained using the protocol described in PEPPI-MS[24]. The fractions (6 µL) were then incorporated into the mass spectrometer with a flow of 20 µL/min. The ion source was NSI, and the detector was an Orbitrap. Mass spectrometry data analysis was performed using TopMSV[25]. The E-value of the detected proteoforms is ~10^{-3}-10^{-4}. The reported proteoforms were identified in two biological replicates of PEPPI-MS. Proteoforms identified in only one of the replicates were discarded.

Results and Discussion

Separation of CK8 proteoforms is possible using whole-cell lysis buffers

We first evaluated the presence of CK8 proteoforms in the MCF7 cell line using top-down mass spectrometry. We identified proteoforms accession #P057878-1, #P05787-2, #F8VQY3, #F8VUG2, and #H0YUB2 (**Fig. 1B**). These findings indicate that the MCF7 cells express both confirmed alternative-splicing isoforms, as well as additional fragments.

We proceeded to cross-evaluate these results using scWB[22], a technique that measures proteoform expression at the single-cell level (**Fig. 1C**). In scWB developed for whole-cell analysis, all cellular compartments are solubilized - including the nuclear compartment - using RIPA cell-lysis buffer, a buffer with a 2% w/v sodium dodecyl sulfate (SDS) content. SDS solubilizes both cytoplasmic and nuclear membranes, and linearizes cellular proteins for mass-based electrophoresis. Using RIPA, we evaluated a breast cancer biomarker panel (CK5/6, CK8, CK14 and CK20), where only CK8 presented proteoforms (**SI Fig. 1**). With CK8, we observe that 10.3% of the single cells present a second proteoform (n=629). Based on the electrophoretic migration distance, the main proteoform observed is posited to be the main CK8 form or isoform (53.7 and 56.6 kDa, respectively, **Fig. 1C**), which aligns with the migration of the reference protein β-tubulin (55 kDa). However, due to the limitations of single-cell electrophoresis in resolving such small differences (here 2.9 kDa or < 12% of total mass)[26], we attribute the other detected proteoform to the fragment #F8VUG2 (30.9 kDa), observed in MCF7 cells via mass spectrometry, and which has an annotated biological function.

To retain the nuclear compartment while assessing proteoforms, we performed fractionated scWB using a cytoplasmic buffer previously used by our team for single-cell DDF for scWB[16–18], consisting of Triton x-100, digitonin, and Tris-Glycine. With these conditions, we did not observe the CK8 proteoform in a population of 800 cells (**Fig. 1D, right panel, SI Fig. 2**). There are two possible explanations for this: a) the proteoform does not properly solubilize with the cytoplasmic buffer or b) the migration of both proteoforms is overlapping, as this native buffer does not contain SDS, thus this buffer preserves native protein structure and protein

charge state. This finding suggests that advancing single-cell proteoform analysis while maintaining nuclear integrity will require the development of new chemical solubilization strategies, thus forming the rationale for the present study.

Nonionic detergents enhance proteoform detection

The composition of the detergent cocktail impacts protein solubilization, especially at the single-cell level. The scWB demands protein solubilization in just a few seconds, because the open microwell format means that diffusion of the concomitantly solubilizing proteins out of the microwell curtails detection sensitivity of the completed scWB[27]. Thus, solubilization times of 100-1000's of seconds are not possible or require alternative strategies, such as droplet encapsulation[28], making the choice of detergent critical to achieve proper protein solubilization. Detergents result in different solubilization efficiencies for each protein species, a product of each protein distinct properties, including charges, hydrophilic and hydrophobic regions, and 3D conformation. Buffers are typically composed of a combination of three commonly used detergent types: anionic, zwitterionic, and nonionic detergents. Anionic detergents, such as SDS, generally destabilize all cellular membranes and thus are not compatible with cell fractionation (i.e., the whole cell lyses)[29]. Zwitterionic detergents, such as urea, are usually mild, but they do partially dissociate the nuclear membrane, allowing DNA fragmentation and migration into the gel (**Fig. 2C**). Nonionic detergents are thus the preferred choice for specific solubilization of the membrane and cytoplasm, since they break lipid-lipid and lipid-protein interactions, but preserve protein-protein interactions intact, or even are biologically active[26]. Given an inability to dissolve protein-protein interactions, non-ionic detergents cannot dissolve the nuclear lamina structure, and consequently maintain nuclei integrity in a manner that makes said nuclei suitable for further analysis.

Here, we evaluated nonionic detergents to determine the efficacy in solubilizing CK8 proteoforms. We used the cytoplasmic buffer as base composition and tested the addition of Brij-35, n-dodecacyl-β-maltosidase (DDM), and IGEPAL CA-630. **Fig. 2A** shows the different intensities of CK8 achieved with each of the buffers. IGEPAL 0.1% yielded the highest mean intensity levels, which we use as proxy to protein solubilization, although the differences were not statistically significant. After solubilization with either of the buffers, we could still observe remnant CK8 inside the nucleus. This could be explained by the presence of CK8 in the nucleus, and also partial solubilization of protein.

Roughly 34% of microwells containing cells show CK8 detection by electrophoresis (**Fig. 2B**), in contrast to β-tubulin, which reached up to a 68% solubilization under some of the conditions (**SI Fig. 3**). Despite the higher solubilization and the stronger signal observed in β-tubulin, the solubilization of β-tubulin protein with either of the buffers was not complete. Protein species require individualized approaches for solubilization[30], thus precluding development of a "universal buffer" that can solubilize most of a diverse physicochemical universe of protein molecules. The electrophoretic migration distance from the protein injection point (i.e., the microwell lip) was measured to be non-uniform across the different buffers (**Fig. 2D**), suggesting that different nonionic detergents facilitate proteoform electrophoretic separation by exploiting distinct migration patterns related to molecular mass, surface charge, and structure.

From the conditions considered, we resolved CK8 proteoforms in two buffers: Brij-35 0.1%, and IGEPAL 0.2%, which led us to combine both detergents to increase proteoform solubilization. This approach increased the percentage of cells with detectable proteoforms to 14.3% (**Fig. 3A-B**), comparable to results with the RIPA buffer. However, Brij-35 has the lowest CK8 solubilization efficiency across the nonionic detergents tested, which reduces the total CK8 solubilization with the Brij-35 0.1% +IGEPAL 0.2% buffer when compared to the IGEPAL 0.2%. This is not the case for β-tubulin, which exhibits poor solubilization with DDM, but the highest with the Brij-35 0.1% + IGEPAL 0.2% buffer (**SI Fig. 3**).

In order to sufficiently resolve the detected CK8 proteoforms, various parameters such as lysis time, buffer temperature, and electric field were evaluated. In all cases, adjusting the parameters involved trade-offs. For CK8, lower solubilization temperatures (55°C) offered significantly higher signal intensity per area; however, solubilization and separation resolution were improved at 85°C. Furthermore, the migration distance of CK8 increased with temperature, likely due to a better solubilization of CK8 filaments (**Fig. 4A-B**). The lysis time did not show a clear correlation with the number of solubilized cells, although 30 s solubilization gave generally the best intensity/area ratio for CK8 (**Fig. 4C**). In the case of β-tubulin, 20 s showed the best overall lysis time based on the median intensity/area of the cells, while 75°C was the best lysing temperature (**SI Fig. 4A-B**).

To maximize the proteoform separation resolution, we analyzed the electrophoretic mobility of the two CK8 proteoforms distinguishable by scWB using Ferguson plots with varying polyacrylamide-gel concentrations (%T) (**Fig. 3C, SI Fig. 5**). Both CK8 proteoforms show similar values for the y-intercept ($y_{full\text{-}length}$=-15x-2.66 and $y_{fragment}$=-13.0x-2.64), suggesting that the use of different %T concentrations in the separation gel will be unlikely to enhance separation resolution. In addition, the non-linearity of the relationship suggests a non-spherical conformation, consistent with reports of CK8 being a filamentous protein[31].

Adjusting the electric field, however, had the largest impact on the separation resolution of the proteoforms (**Fig. 3D-F**). At 30 V/cm, separation resolution was the largest (R_s=0.94, calculated as $R_s=2(d_2-d_1)/(w_1+w_2)$, where d is the distance to the peak, and w is the peak width) and the highest number of proteoforms detected as a percentage of total electrophoresed cells. An applied electric field of 25 V/cm gave an R_s=0.7, whereas 40 V/cm yielded R_s=0.85. Conversely, at 20 V/cm proteoforms were not resolvable, and overall band intensity was weak. The electrical field also impacted the number of detected proteoforms, with 30 V/cm showing the highest percentage (**Fig. 3E**). In cases of poor separation resolution, the presence of proteoforms can only be identified by a skewed Gaussian peak in comparison with a compact circular band observed in cells with only one proteoform.

Nuclear stability after DDF and electrophoresis depends on cell line

In addition to proteoform solubilization, for a DDF protocol to be effective, the fractionation approach must preserve the physical and chemical integrity of each nucleus. While nonionic detergents are mild and preserve most protein-protein interactions, this effect might vary across different cell lines. **Fig. 5** illustrates the migration of CK8 and β-tubulin in three different breast cancer cell lines

(MCF7, SKBR3, and MDA-MB-231), confirming the solubilization of proteins under the selected conditions. The migration of CK8 corresponds to the expected values, with no CK8 detected in the basal cell line, MDA-MB-231, while luminal cell lines (MCF7 and SKBR3) showed migration[16]. No CK8 fragments were observed in SKBR3.

To assess nuclear stability, we used the histone H3 as a marker. Histones are an integral part of the chromatin structure, playing a key role in DNA condensation. The absence of histone migration into the gel indicates that histones still remain confined in the nucleus, implying nuclear conservation. Experimentally, we observe that H3 remains retained within the microwell, suggesting preserved nuclear stability[32]. For comparison, **SI Fig. 6** depicts a fragmented nucleus of a transfected MCF7 cell, where the nuclear content is migrating inside of the gel, and thus the nuclear structure is shown to be compromised. This highlights the importance of matching cell lysis buffer composition to cell type in achieving reliable nuclear preservation in DDF. In addition, we observe that the DNA, similarly to the H3 histone, is confirmed in the microwell, as shown in **Fig. 2C**.

Conclusions

The diversity of physicochemical properties of protein molecules demands customization and optimization of lysis conditions to achieve an effective protein separation, especially at the single-cell level. Here, we presented an approach that optimizes the solubilization and detection of CK8 proteoforms while preserving nuclear integrity. By selecting nonionic detergents and adjusting electrophoretic conditions, this method enables enhanced separation and visualization of proteoforms across different cell lines.

Proteins are challenging to solubilize due to their wide range of physicochemical properties. This issue parallels challenges in crystallography, where obtaining protein crystals requires extensive testing of different conditions. Similarly, successful selective lysis and proteoform separation in electrophoretic gels will depend on the particular conditions employed. Such selectivity is not required for total cell solubilization (no nuclear isolation), and thus, it is easier to achieve.

The approach described here provides a platform to investigate the biological impact of CK8 fragments on single-cells while retaining the nuclear compartment. The nuclear preservation maintains the integrity of DNA and nuclear proteins, and may also conserve portions of RNA, enabling a multi-omic analysis such as transcriptomic, genomic, epigenetic analysis in addition to targeted protein expression. CK8 is an excellent example for this approach, as it presents several transcript products of alternative splicing, but it also shows protein variability product of protease activity. While ultimate confirmation of proteoform identity benefits from mass spectrometry, we observe that both whole-cell lysis (RIPA) and cytoplasmic lysis (DDF) yield CK8 peaks with comparable molecular mass and pI with that of the alternative spliced forms (molecular mass=53.7 and 56.6 kDa, and pI=5.52 and 5.37 as calculated by the ExPASy Compute pI/Mw tool[33]). Although these alternative splicing products and protein fragments have been linked to distinct disease states, their precise biological significance remains largely unexplored. While the DDF scWB presented here enables the examination of many of these possibilities, it still presents some limitations. For instance, the separation of closely sized spliced proteoforms remains a challenge, and the percentage of solubilized proteins remains low in all tested conditions. Nonetheless, DDF scWB represents a step forward in aiding single-cell proteoform analysis, enabling protein characterization while preserving the integrity of cellular compartments for downstream multi omic investigations.

AUTHOR INFORMATION

Corresponding Author

* aeh@berkeley.edu

Author Contributions

The manuscript was written through contributions of all authors. All authors have given approval to the final version of the manuscript.

ACKNOWLEDGMENT

A.E.H. acknowledges financial support from the Investigator Program of the Chan Zuckerberg Biohub San Francisco and the US National Institutes of Health (NIH R01CA20301). A.F.K. acknowledges support from the Swiss National Science Foundation (SNSF) Postdoc Mobility fellowship. The photolithography was performed in the QB3 Biomolecular Nanotechnology Center and mass spectrometry was performed in the QB3 Vincent J. Coates Proteomics/Mass Spectrometry Laboratory by Dr. Robert Maxwell, both at UC Berkeley.

REFERENCES

(1) *KRT8 protein expression summary - The Human Protein Atlas*. https://www.proteinatlas.org/ENSG00000170421-KRT8 (accessed 2024-10-25).

(2) Sun, M.-Z.; Dang, S.-S.; Wang, W.-J.; Jia, X.-L.; Zhai, S.; Zhang, X.; Li, M.; Li, Y.-P.; Xun, M. Cytokeratin 8 Is Increased in Hepatitis C Virus Cells and Its Ectopic Expression Induces Apoptosis of SMMC7721 Cells. *World Journal of Gastroenterology : WJG* **2013**, *19* (37), 6178. https://doi.org/10.3748/wjg.v19.i37.6178.

(3) De Conto, F.; Conversano, F.; Razin, S. V.; Belletti, S.; Arcangeletti, M. C.; Chezzi, C.; Calderaro, A. Host-Cell Dependent Role of Phosphorylated Keratin 8 during Influenza A/NWS/33 Virus (H1N1) Infection in Mammalian Cells. *Virus Research* **2021**, *295*, 198333. https://doi.org/10.1016/j.virusres.2021.198333.

(4) Cortese, M.; Goellner, S.; Acosta, E. G.; Neufeldt, C. J.; Oleksiuk, O.; Lampe, M.; Haselmann, U.; Funaya, C.; Schieber, N.; Ronchi, P.; Schorb, M.; Pruunsild, P.; Schwab, Y.; Chatel-Chaix, L.; Ruggieri, A.; Bartenschlager, R. Ultrastructural Characterization of Zika Virus Replication Factories. *Cell Reports* **2017**, *18* (9), 2113–2123. https://doi.org/10.1016/j.celrep.2017.02.014.

(5) Murray, K. A.; Hughes, M. P.; Hu, C. J.; Sawaya, M. R.; Salwinski, L.; Pan, H.; French, S. W.; Seidler, P. M.; Eisenberg, D. S. Identifying Amyloid-Related Diseases by Mapping Mutations in Low-Complexity Protein Domains to Pathologies. *Nat Struct Mol Biol* **2022**, *29* (6), 529–536. https://doi.org/10.1038/s41594-022-00774-y.

(6) Cho, Y. H.; Jung, S. I.; Hwang, E. C. Chapter 31 - Novel and Emerging Surveillance Markers for Bladder Cancer. In *Bladder Cancer*; Ku, J. H., Ed.; Academic Press, 2018; pp 599–612. https://doi.org/10.1016/B978-0-12-809939-1.00031-X.

(7) Fukunaga, Y.; Bandoh, S.; Fujita, J.; Yang, Y.; Ueda, Y.; Hojo, S.; Dohmoto, K.; Tojo, Y.; Takahara, J.; Ishida, T. Expression of Cytokeratin 8 in Lung Cancer Cell Lines and Measurement of Serum Cytokeratin 8 in Lung Cancer Patients. *Lung Cancer* **2002**, *38* (1), 31–38. https://doi.org/10.1016/S0169-5002(02)00109-5.

(8) Fomitcheva-Khartchenko, A.; Rapsomaniki, M. A.; Sobottka, B.; Schraml, P.; Kaigala, G. V. Spatial Protein Heterogeneity Analysis in Frozen Tissues to Evaluate Tumor Heterogeneity. *PLoS ONE* **2021**, *16* (11), e0259332. https://doi.org/10.1371/journal.pone.0259332.

(9) Albaret, M. A.; Paré, A.; Malet, L.; De Souza, G.; Lavergne, E.; Goga, D.; De Pinieux, G.; Castellier, C.; Swalduz, A.; Robin, V.; Lavergne, V.; Mertani, H.-C.; Treilleux, I.; Vermot-Desroches, C.; Diaz, J.-J.; Saintigny, P. Combined Proteomic and Transcriptomic Approaches Reveal Externalized Keratin 8 as a Potential Therapeutic Target Involved in Invasiveness of Head and Neck Cancers. *Translational Oncology* **2021**, *14* (1), 100878. https://doi.org/10.1016/j.tranon.2020.100878.

(10) Gharib, T. G.; Chen, G.; Wang, H.; Huang, C.-C.; Prescott, M. S.; Shedden, K.; Misek, D. E.; Thomas, D. G.; Giordano, T. J.; Taylor, J. M. G.; Kardiat, S.; Yee, J.; Orringer, M. B.; Hanash, S.; Beer, D. G. Proteomic Analysis of Cytokeratin Isoforms Uncovers Association with Survival in Lung Adenocarcinoma. *Neoplasia* **2002**, *4* (5), 440–448. https://doi.org/10.1038/sj.neo.7900257.

(11) Li, Z.; Zhang, B.; Chan, J. J.; Tabatabaeian, H.; Tong, Q. Y.; Chew, X. H.; Fan, X.; Driguez, P.; Chan, C.; Cheong, F.; Wang, S.; Siew, B. E.; Tan, I. J.-W.; Lee, K.-Y.; Lieske, B.; Cheong, W.-K.; Kappei, D.; Tan, K.-K.; Gao, X.; Tay, Y. An Isoform-Resolution Transcriptomic Atlas of Colorectal Cancer from Long-Read Single-Cell Sequencing. *Cell Genomics* **2024**, *4* (9). https://doi.org/10.1016/j.xgen.2024.100641.

(12) *KRT8 - Keratin, type II cytoskeletal 8 - Homo sapiens (Human) | UniProtKB | UniProt*. https://www.uniprot.org/uniprotkb/P05787/entry#sequences (accessed 2024-10-25).

(13) Ditzel, H. J.; Strik, M. C. M.; Larsen, M. K.; Willis, A. C.; Waseem, A.; Kejling, K.; Jensenius, J. C. Cancer-Associated Cleavage of Cytokeratin 8/18 Heterotypic Complexes Exposes a Neoepitope in Human Adenocarcinomas *. *Journal of Biological Chemistry* **2002**, *277* (24), 21712–21722. https://doi.org/10.1074/jbc.M202140200.

(14) Liao, P.-C.; Bergamini, C.; Fato, R.; Pon, L. A.; Pallotti, F. Isolation of Mitochondria from Cells and Tissues. *Methods Cell Biol* **2020**, *155*, 3–31. https://doi.org/10.1016/bs.mcb.2019.10.002.

(15) Hubbard, W. B.; Harwood, C. L.; Prajapati, P.; Springer, J. E.; Saatman, K. E.; Sullivan, P. G. Fractionated Mitochondrial Magnetic Separation for Isolation of Synaptic Mitochondria from Brain Tissue. *Sci Rep* **2019**, *9* (1), 9656. https://doi.org/10.1038/s41598-019-45568-3.

(16) Yamauchi, K. A.; Herr, A. E. Subcellular Western Blotting of Single Cells. *Microsyst Nanoeng* **2017**, *3* (1), 1–9. https://doi.org/10.1038/micronano.2016.79.

(17) Rosàs-Canyelles, E.; Modzelewski, A. J.; Martinez, A. E. G.; Geldert, A.; Gopal, A.; He, L.; Herr, A. E. Multimodal Detection of Protein Isoforms and Nucleic Acids from Low Starting Cell Numbers. *Lab Chip* **2021**, *21* (12), 2427–2436. https://doi.org/10.1039/D1LC00073J.

(18) Rosàs-Canyelles, E.; Modzelewski, A. J.; Geldert, A.; He, L.; Herr, A. E. Multimodal Detection of Protein Isoforms and Nucleic Acids from Mouse Pre-Implantation Embryos. *Nat Protoc* **2021**, *16* (2), 1062–1088. https://doi.org/10.1038/s41596-020-00449-2.

(19) Kayo, S.; Bahnemann, J.; Klauser, M.; Pörtner, R.; Zeng, A.-P. A Microfluidic Device for Immuno-Affinity-Based Separation of Mitochondria from Cell Culture. *Lab on a Chip* **2013**, *13* (22), 4467–4475. https://doi.org/10.1039/C3LC50739D.

(20) Tesauro, C.; Ferrando, B.; Ma, X.; Jepsen, M. L.; Ivarsen, A. K. R.; Frøhlich, R.; Stevnsner, T.; Knudsen, B. R.; Ho, Y. P. Isolation of Functional Mitochondria by Inertial Microfluidics – a New Method to Sort Intracellular Organelles from a Small Scale Biological Sample. *RSC Adv.* **2017**, *7* (38), 23735–23741. https://doi.org/10.1039/C7RA03384B.

(21) Lee, C.; Chen, Y.; Wang, P.; Wallace, D. C.; Burke, P. J. A Three-Dimensional Printed Inertial Microfluidic Platform for Isolation of Minute Quantities of Vital Mitochondria. *Anal. Chem.* **2022**, *94* (19), 6930–6938. https://doi.org/10.1021/acs.analchem.1c03244.

(22) Hughes, A. J.; Spelke, D. P.; Xu, Z.; Kang, C.-C.; Schaffer, D. V.; Herr, A. E. Single-Cell Western Blotting. *Nat Meth* **2014**, *11* (7), 749–755.

(23) Gopal, A.; Herr, A. E. Segmentation-based Analysis of Single-cell Immunoblots. *Electrophoresis* **2021**, *42* (20), 2070–2080. https://doi.org/10.1002/elps.202100144.

(24) Takemori, A.; Butcher, D. S.; Harman, V. M.; Brownridge, P.; Shima, K.; Higo, D.; Ishizaki, J.; Hasegawa, H.; Suzuki, J.; Yamashita, M.; Loo, J. A.; Loo, R. R. O.; Beynon, R. J.; Anderson, L. C.; Takemori, N. PEPPI-MS: Polyacrylamide-Gel-Based Prefractionation for Analysis of Intact Proteoforms and Protein Complexes by Mass Spectrometry. *J. Proteome Res.* **2020**, *19* (9), 3779–3791. https://doi.org/10.1021/acs.jproteome.0c00303.

(25) Choi, I. K.; Jiang, T.; Kankara, S. R.; Wu, S.; Liu, X. TopMSV: A Web-Based Tool for Top-Down Mass Spectrometry Data Visualization. *J. Am. Soc. Mass Spectrom.* **2021**, *32* (6), 1312–1318. https://doi.org/10.1021/jasms.0c00460.

(26) Vlassakis, J.; Herr, A. E. Joule Heating-Induced Dispersion in Open Microfluidic Electrophoretic Cytometry. *Anal. Chem.* **2017**, *89* (23), 12787–12796. https://doi.org/10.1021/acs.analchem.7b03096.

(27) Su, E. J.; Jeeawoody, S.; Herr, A. E. Protein Diffusion from Microwells with Contrasting Hydrogel Domains. *APL Bioengineering* **2019**, *3* (2), 026101. https://doi.org/10.1063/1.5078650.

(28) Liu, Y.; Herr, A. E. DropBlot: Single-Cell Western Blotting of Chemically Fixed Cancer Cells. *Nat Commun* **2024**, *15* (1), 5888. https://doi.org/10.1038/s41467-024-50046-0.

(29) Le Maire, M.; Champeil, P.; Møller, J. V. Interaction of Membrane Proteins and Lipids with Solubilizing Detergents. *Biochimica et Biophysica Acta (BBA) - Biomembranes* **2000**, *1508* (1–2), 86–111. https://doi.org/10.1016/S0304-4157(00)00010-1.

(30) Kundlacz, T.; Bender, J.; Schmidt, C. Effects of Non-Ionic and Zwitterionic Detergents on Soluble Proteins during Native Mass Spectrometry Experiments. *International Journal of Mass Spectrometry* **2021**, *468*, 116652. https://doi.org/10.1016/j.ijms.2021.116652.

(31) Kuburich, N. A.; den Hollander, P.; Pietz, J. T.; Mani, S. A. Vimentin and Cytokeratin: Good Alone, Bad Together. *Seminars in Cancer Biology* **2022**, *86*, 816–826. https://doi.org/10.1016/j.semcancer.2021.12.006.

(32) Müller, L. Protocol to Determine the Subcellular Localization of Protein Interactions in Murine Keratinocytes. *STAR Protocols* **2023**, *4* (2), 102309. https://doi.org/10.1016/j.xpro.2023.102309.

(33) Gasteiger, E. ExPASy: The Proteomics Server for in-Depth Protein Knowledge and Analysis. *Nucleic Acids Research* **2003**, *31* (13), 3784–3788. https://doi.org/10.1093/nar/gkg563.

Figure 1. CK8 proteoform presence in MCF7 cells. A) Scheme of *KRT8* transcripts and the corresponding protein accession #. B) Schematic representing the proteoforms detected by top-down mass spectrometry in bulk MCF7 cell suspension. Regions of sequence alignment identified by the Clustal Omega program from UniProt are highlighted in light purple, while dark purple indicates distinct sequences. In addition, the scheme shows the proteoforms with known function and their molecular mass. C) Workflow schematic for scWB with differential detergent fractionation (DDF). Steps include: gravity-based cell settling into microwells, DDF lysis settled cells electrophoresis (EP) to separate proteoforms by molecular mass with subsequent light-based immobilization of protein to the benzophenone-methacrylate containing polyacrylamide gel, and antibody-based probing for fluorescence detection. D) Micrograph representing a scWB of CK8 using RIPA buffer (solubilization of both nuclear and cytoplasmic proteins), showing CK8 presents proteoforms in 10.3% of the analyzed cells (n=629). The purple curve represents the single proteoform band, while the blue curve represents the proteoforms. E) No CK8 proteoforms are detected when performing DDF with a cytoplasmic buffer (n=800). Scale bar: 30 µm.

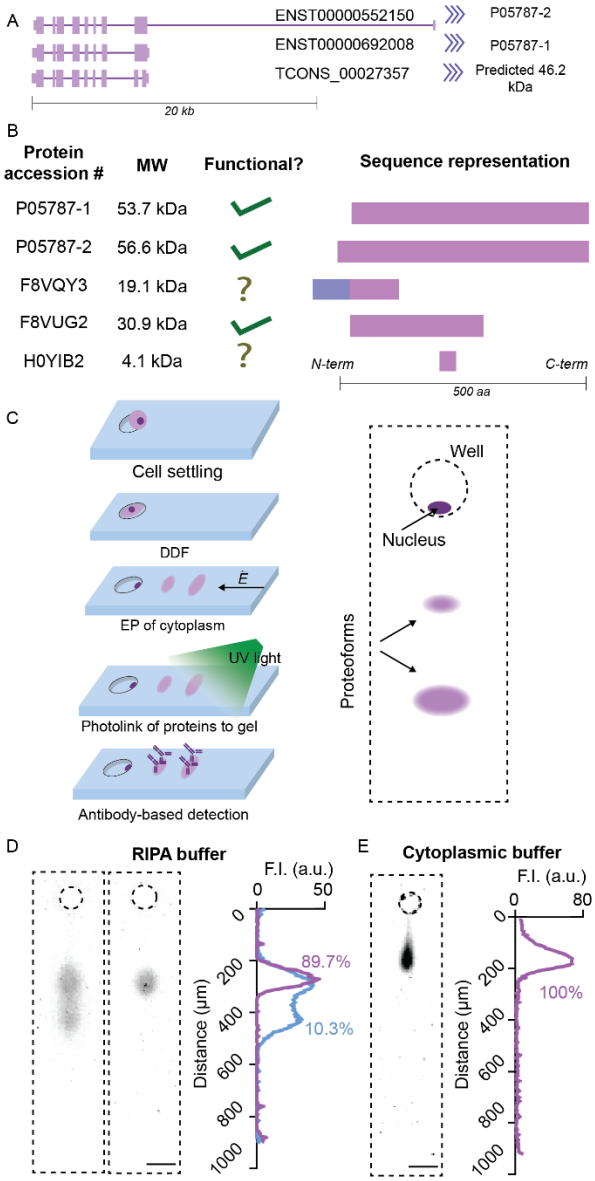

Figure 2. Distinct solubilization of CK8 based on nonionic detergent addition. A) Violin plot representing intensity profiles normalized by the total area of the protein spot for CK8 across tested buffers. The number of microwells with cells in the scWB ranges from 14 to 124. B) Bar plot representing the percentage of solubilized cells using different detergents. C) Micrograph representing a microwell stained for DNA using SYBR gold after scWB. The left image shows a preserved nucleus (use of Brij-35 0.1%+IGEPAL 0.2% buffer), while the right band has fragmented DNA that penetrates into the gel (use of urea 0.1% buffer). D) Bar plot showing CK8 migration distance into the gel. Large error bars are likely caused by uneven heating across the gel, resulting in differences of migration distance across the gel.

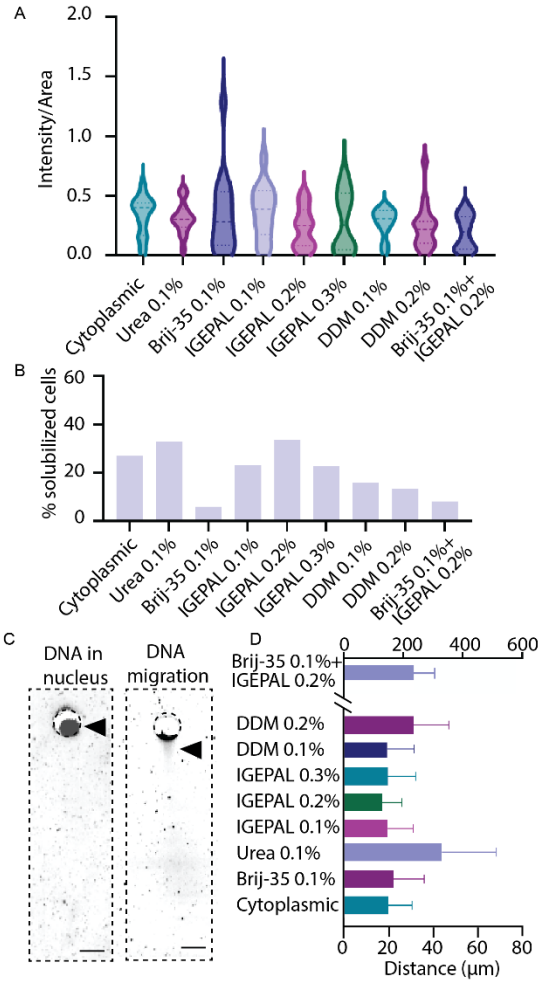

Figure 3. Effects of the electrical field on proteoform separation. A) Micrographs demonstrating representative CK8 proteoforms lysed at 85°C and electrophoresed using 30 V/cm. B) Percentage of cells with detectable proteoforms per buffer where proteoforms were visualized (total cells with migration into the gel n=26 for Brij-35 0.1%, n=132 for IGEPAL 0.2%, and n=35 for Brij-35 0.1%+IGEPAL 0.2%). C) Micrograph matrix showing proteoforms across two electric fields and four %T. D) Plot showing the separation resolution of the proteoforms across different electric fields. E) Micrographs of the corresponding plots in (D). Electrophoresis times were adjusted to 90, 70, 50, and 40 s for 20 to 40 V/cm, respectively, as the same electrophoresis time would not separate the proteoforms under all conditions. F) Percentage of cells showing proteoforms at multiple electric fields.

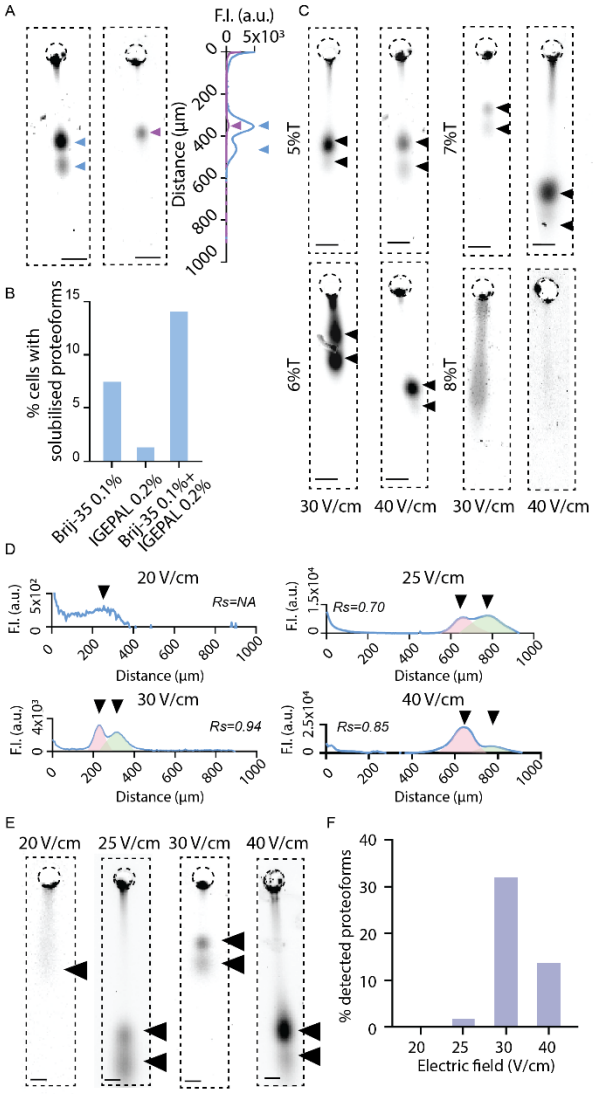

Figure 4. Impact of buffer temperature and lysis time on CK8 solubilization. (A) Optimization of buffer temperature for CK8. Lysis time was 30s and electrophoresis time was 30 s, gels were 7%T. For each temperature, n=78, 31, 78, and 40, respectively. (B) Plot showing the migration distance of the CK8 bands with increasing temperatures. The right panel shows that the solubilization of the protein is better at higher temperatures. Scale bar: 30 µm. (C) Optimization of buffer lysis time for CK8. Electrophoresis time was 30s, gels were 7%T, and the buffer temperature was 55°C. For each lysis time, n=134, 78, 153, 56, and 29, respectively. Significance is as follows: * $P \leq 0.05$, ** $P \leq 0.01$, *** $P \leq 0.001$, **** $P \leq 0.0001$.

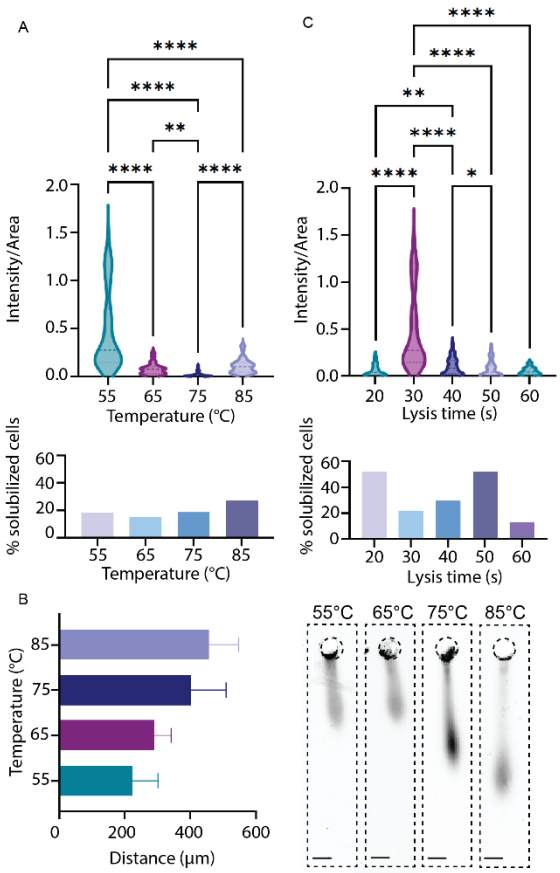
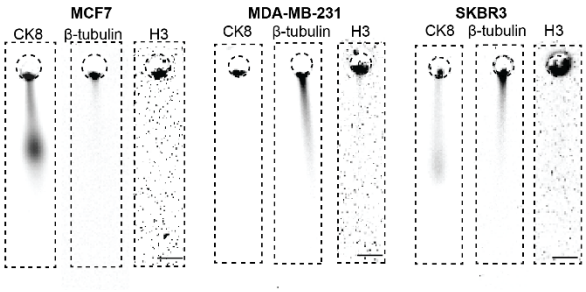
Figure 5. Effects of the buffer on nuclear integrity on MCF7, MDA-MB-231, and SKBR3 cell lines. Cytoplasmic proteins such as CK8 and β-tubulin show a migration into the gel, while histone H3, a nuclear marker intercalated in the DNA does not inject into the gel. The gain was substantially increased for imaging in H3 to ensure that no migration of protein is observed, and thus noise is observed in these micrographs. Scale bar: 30 μm.